Supplementary Information for

Sustainable high-energy aqueous zinc–manganese dioxide batteries enabled by stress-governed metal electrodeposition and fast zinc diffusivity

Authors: Huijun Yang[1]†, Ruijie Zhu[2]†, Yang Yang[3], Ziyang Lu[3], Zhi Chang[1], Ping He[4], Chunyu Zhu[5], Sho Kitano[6], Yoshitaka Aoki[6], Hiroki Habazaki[6], Haoshen Zhou[1,4]*

Affiliations:

[1]Energy Technology Research Institute, National Institute of Advanced Industrial Science and Technology, Umezono, Tsukuba 305-8568, Japan.

[2]Graduate School of Chemical Sciences and Engineering, Hokkaido University, Sapporo, Hokkaido 060-8628, Japan.

[3]Graduate School of System and Information Engineering, University of Tsukuba, 1-1-1, Tennoudai, Tsukuba 305-8573, Japan.

[4]Center of Energy Storage Materials Technology, College of Engineering and Applied Sciences, Jiangsu Key Laboratory of Artificial Functional Materials, National Laboratory of Solid State Microstructures, and Collaborative Innovation Center of Advanced Microstructures, Nanjing University, Nanjing 210093, China.

[5]School of Electrical and Power Engineering, China University of Mining and Technology, Xuzhou 221116, China.

[6]Division of Applied Chemistry, Faculty of Engineering, Hokkaido University, Sapporo, Hokkaido 060-8628, Japan.

*Correspondence to: hszhou@nju.edu.cn

†These authors contributed equally to this work.

Methods

Materials. The hydrophilic polyvinylidene difluoride-type membrane (VVLP, pore size: 0.1 μm) was purchased from Mrckmillipore company. The VVLP and glass fiber (GF/A, Whatman-100) filters were cut-off into plates with diameter of 16 mm as separators without further treatment. Zinc (Zn) foil (Nilaco company, 100 μm, purity>99.99%) was polished to remove contaminants and oxide coating in ethanol solutions and was cut-off into plates with diameter of 10 mm or large-area plates (7 cm×5 cm)for pouch cells. Zn paper (Nilaco company, 50 μm, purity>99.99%) was used to observe the Zn electrodeposition morphology to prove its sensitivity to exchange current density in fig. S10. $ZnSO_4.7H_2O$ and $MnSO_4.H_2O$ were purchased from Tokyo Chemical Industry for electrolyte preparation.

Electrolyte. Dissolving $ZnSO_4.7H_2O$ into deionized water to prepare electrolyte (2 mol L^{-1} $ZnSO_4$ water solution) for symmetric Zn||Zn, Zn||Cu, Zn||carbon paper half cells. Dissolving $ZnSO_4.7H_2O$ and $MnSO_4.H_2O$ into deionized water to prepare electrolyte (2 mol L^{-1} $ZnSO_4$ +0.1 mol L^{-1} $MnSO_4$ water solution) for Zn-MnO_2 cells.

Electrode. The MnO_2 electrode was synthesized through a one-step hydrothermal method. Dissolving $MnSO_4.H_2O$ and $KMnO_4$ (Wako Chemical Industry) into deionized water with a mole ratio of 10:4. The as-prepared water solution was fully stirred and transferred into Teflon for hydrothermal reaction (12 hours at 140ºC). The as-obtained powder was fully washed by ethanol solutions until the filtrates turns into colorless and then was transferred into vacuum oven (24 hours at 90ºC) to remove the absorbed solvents. The as-obtained α-MnO_2 was mixed with carbon black (ketjen black, KB) and poly(tetrafluoroethylene) (PTFE suspension, 10 wt%) in water/ethanol solutions at mass ratio of 80:17:3 to prepare a free-standing electrode and press it onto carbon paper current collector.

Cell assembly and electrochemical characterization. All test CR-2032 coin-cells (Hohsen Corp) in this study were assembled in the ambient environment without special attention. All the cells were remained on open circuit for 4 hours before electrochemical characterizations. The symmetric Zn/Zn cells was assembled by stack of Zn plate, GF or VVLP separator and Zn plate with 40 μL 2 mol L^{-1} $ZnSO_4$ water electrolyte. The galvanostatic charge-discharge tests were carried out in Neware battery test system (Neware Technology Co.) at 25°C. By applied constant current density (mA cm^{-2}), the cyclic life and over-potential of cells were used to evaluate the Zn metal plating/stripping performance.

Changing one Zn plate into Cu or carbon paper plates Zn||Cu and Zn||carbon paper half cells was carried out. In the test protocol, the Coulombic Efficiency (CE) is the ratio of capacity during stripping process (cut-off potential at 0.5 V, *vs.* Zn/Zn^{2+}) to the electrodeposited capacity of Zn on current collectors (controlled by current density and plating time). The initial CE, average CE, cycle number and overpotential were used to evaluate the cell performance.

The Zn-MnO_2 coin cells was assembled by stack of Zn plate, GF or VVLP separator and MnO_2 electrode with 40 μL 2 mol L^{-1} $ZnSO_4$ +0.1 mol L^{-1} $MnSO_4$ water solution. All the Zn-MnO_2 cells were measured under constant current constant voltage (CCCV) test protocol within 0.8~1.8 V, *vs.* Zn/Zn^{2+}.

The Zn-MnO_2 pouch cells were assembled in the air environment with the same electrodes, electrolyte, and inner cross structure (fig. S29 and S30). The active electrode area is controlled by 7 cm×5 cm, with three layers and an Al-plastic film package in the whole pouch cell. Generally, zinc plate (thickness, 100 μL) was used to pair with high-loading MnO_2 cathode (active MnO_2 loading: 52.0 mg cm^{-2}) in one pouch cell. To reduce the weight, the electrodeposited Zn (ca. 40 μm) on carbon paper current collector was used as the composited anode.

The Electrochemical impedance spectra (EIS) of symmetric Zn cells were measured in Potentiostat/Galvanostat PGSTAT30, Autolab Co. Ltd., Netherlands with the frequency ranging from 100 kHz to 0.1 Hz. Besides, the ionic conductivity of different samples was calculated by ohmic resistance. The ionic conductivity σ was obtained by Equation S1, where *l* is the thickness of the sample, *R* is the ohmic resistance and *A* is the surface area of the sample, respectively.

$\sigma = \frac{l}{R \times A}$ *(Equation S1)*

Characterization of materials

(1) Mechanical test. Uniaxial tensile measurements of GF and VVLP separators were performed by a tensile-compressive tester (INSTRON 5965, Instron Co.). All the dumbbell shaped samples were stretched along the length direction at an extension rate of 100 mm min^{-1}. Uniaxial compress tests were performed by using a compressive tester (Tensilon RTC-1310A, Orientec Co). Sample was firstly cut to a disk shape with a diameter of 10 mm before test. The compression rate was set to 0.1y mm min^{-1}, where the y is the thickness of the sample.

(2) *In-situ* optical cell was designed to observe Zn electrodeposition under the condition of no separator. The optical window of cell gives a cross-section sight on the electrode surface with the galvanostatic electrochemical process.

(3) Scanning Electron Microscope (SEM) measurement and energy dispersive spectroscopy (EDS) measurement were conducted on ZEISS Sigma 500 machine. The electrodes harvested from cells were rinsed several times in dimethoxyethane (DME) solution to remove the precipitated residues in the surface. Prior to the final SEM measurements, all electrodes should dry in the glove box to fully evaporate solvent. The SEM images and EDS distribution would not be damaged during the preparation period.

(4) In plane X-ray diffraction (XRD) patterns of cycled Zn plates were obtained by using an X-ray diffractometer (Rigaku RINT2000 Ultima) using Cu Ka radiation. The cycled Zn plates were plating one time at controlled current and time and underwent the similar wash procedure with SEM characterization.

(5) Atomic force microscopy (AFM) observation of cycled Zn plates was conducted on an AFM machine (Hitachi, NanonaviSII by using the dynamic force mode (DFM). The wash procedure of Zn plates is same with previous characterization.

(6) The laser scanning confocal microscope (LSCM, Lasertec Co. 1LM21D) and its 3D morphology reconstruction were conducted for cycled Zn plates. The narrow laser beam of light can illuminate the visual field and can detect each point. 3D reconstruction of the images gives the distribution of different depths.

Simulation study

1. Distribution of relaxations times (DRT) simulation was conducted by using the DRT tools, which is a block of MATLAB.

2. COMSOL Multiphysics was used to simulate the diffusion controlled dendritic crystal growth. A 2D model based on level-set method was employed as shown in fig. S9. Here, the flux of Zn^{2+} is controlled by Fick's law (Equation S2):

$\frac{\partial c_{Zn^{2+}}}{\partial t} = \nabla \cdot (D \nabla c_{Zn^{2+}})$ *(Equation S2)*

where c_{Zn2+} is the concentration of Zn ion, *t* is the time and *D* is the diffusion coefficient of the Zn ion, respectively.

The deposition of Zn metal is the result of the reaction (Equation S3):

$Zn^{2+} + 2e \longrightarrow Zn^{0}$ *(Equation S3)*

The level-set-interface is set between the Zn foil and the electrolyte while the growth of Zn crystal leads to a moving boundary scenario, and thus the formation of dendritic Zn growth can be tracked. The initial value of the level set variable is 1 in the electrolyte phase, while in the deposition region is 0. The level set variable is governed by the velocity field of the diffusive Zn^{2+} flux (Equation S4):

$$\overrightarrow{u_x} = -D\frac{\partial c_{Zn^{2+}}}{\partial x}\cdot\left(\frac{nM_{Zn}}{\rho_{Zn}}\right) \quad \textit{(Equation S4)}$$
$$\overrightarrow{u_y} = -D\frac{\partial c_{Zn^{2+}}}{\partial y}\cdot\left(\frac{nM_{Zn}}{\rho_{Zn}}\right)$$

where M_{Zn} is the molar mass of zinc and ρ_{Zn} is the density of zinc metal.

The interface thickness is set as ((Equation S5):

$$\varepsilon_{ls} = \frac{h_{\max}}{16} \quad \textit{(Equation S5)}$$

where h_{max} is the maximum mesh size.

The model is based on the Transport of Diluted Species interface. The used parameters are summarized as below:

$D = 3.68 \times 10^{-10}$ m^2 s^{-1} (*1*)
$c_{Zn2+} = 2000$ mol m^{-3}
$M_{Zn} = 65.38$ g mol^{-1}
$\rho_{Zn} = 7.14 \times 10^{-3}$ kg m^{-3}

Supplementary figures

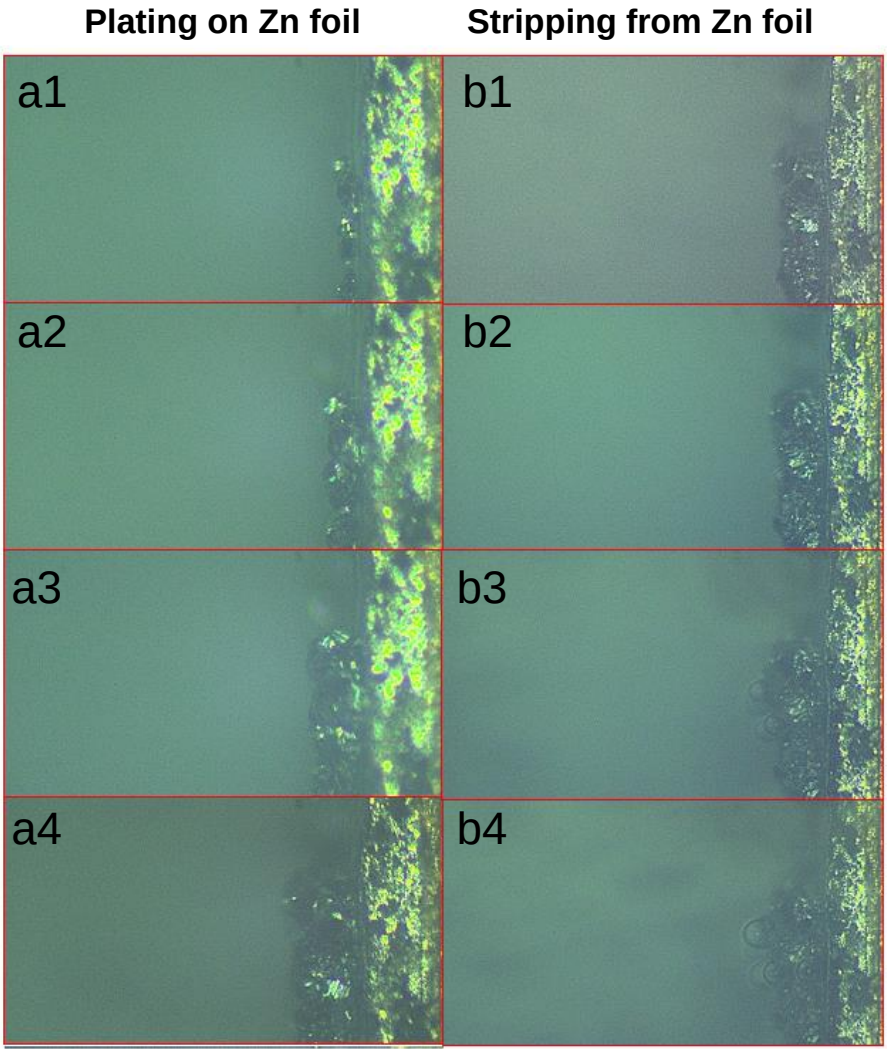

Fig. S1. In-situ optical observation of Zn electrodeposition/dissolution process in cell without separator. The distance between two Zn plates is enough for dendrite growth. This Zn electrodeposition can be regarded as a model without any external stress and the overcrowding Zn accumulation provides internal stress and in turn flatten the surface. a1-a4 pictures belong to plating process, where diversity-oriented Zn electrodeposition causes dendrite. b1-b4 pictures are collected during stripping process, where some dendritic Zn cannot be fully dissolved.

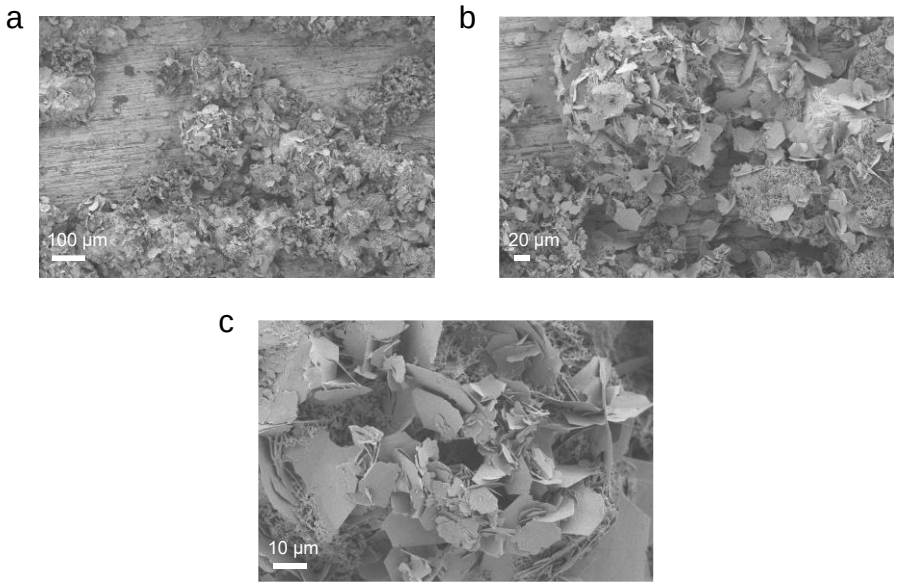

Fig. S2. SEM observation of dendritic Zn electrodeposition in the cell without separator.

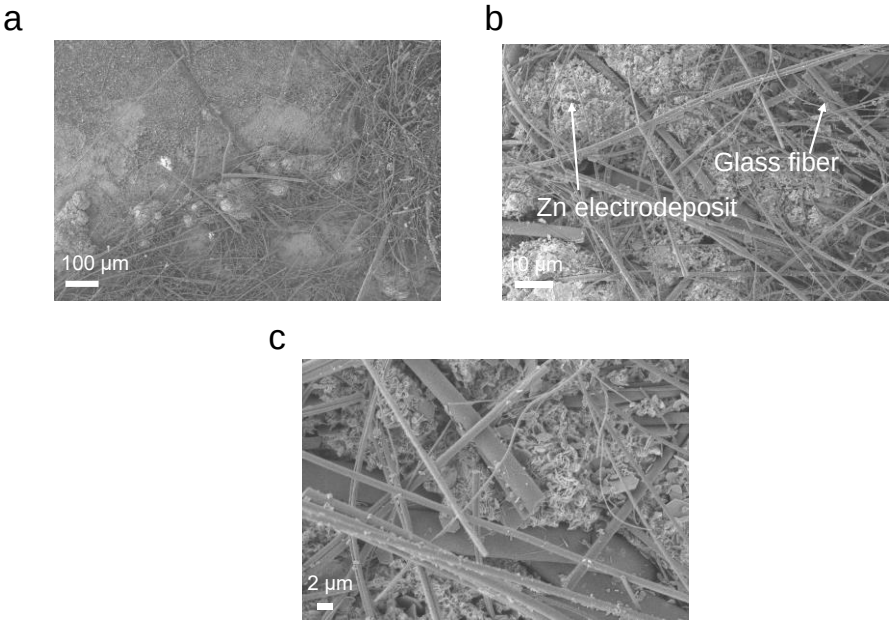

Fig. S3. SEM observation of dendritic Zn electrodeposition process in the cell with glass separator. It indicates the whole space of fiber structure was occupied by Zn dendrite. Glass fiber is regard as the most common separator because of its hydrophilic properties but seems too fragile to shield the growth of Zn dendrite.

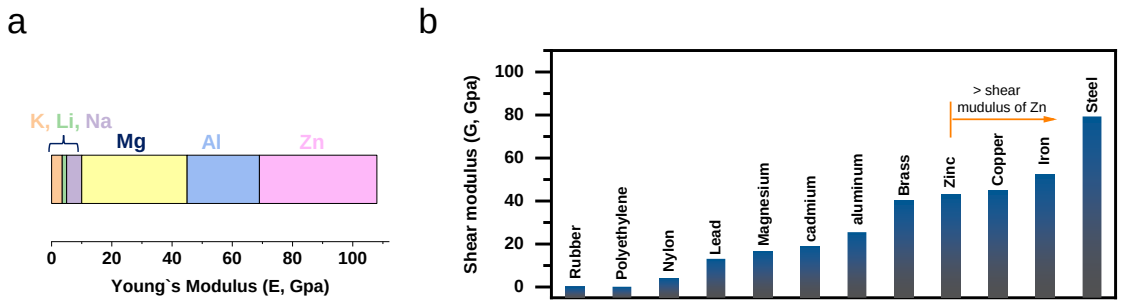

Fig. S4. (a) Young`s Modulus of common metal anodes. (b) Shear modulus of common materials. According to the theoretical assumption of relying mechanical suppression effect, there is very few suitable materials to have high shear modulus.

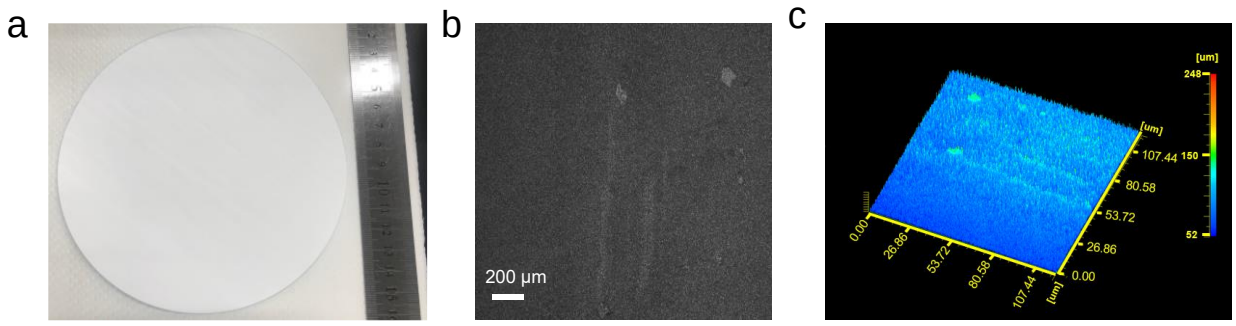

Fig. S5. Optical and SEM observation of VVLP separator. (a) Optical picture. (b) SEM image. (c) Reconstructed 3D topography.

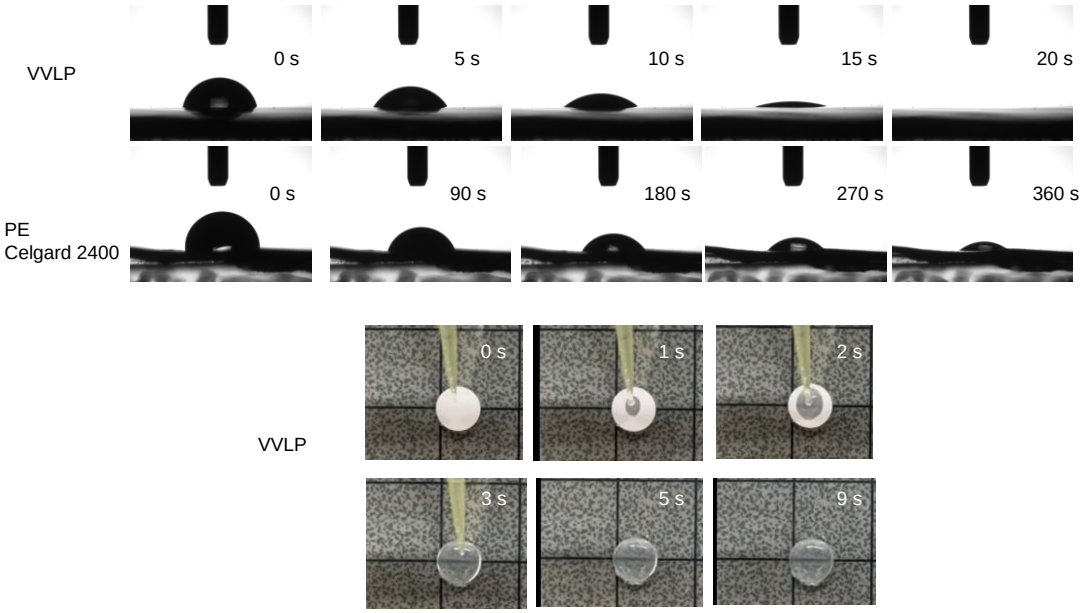

Fig. S6. The contact angle when 2M $ZnSO_4$ aqueous electrolyte dropped on VVLP separator and PE (Celgard separator) surface and the digital photo.

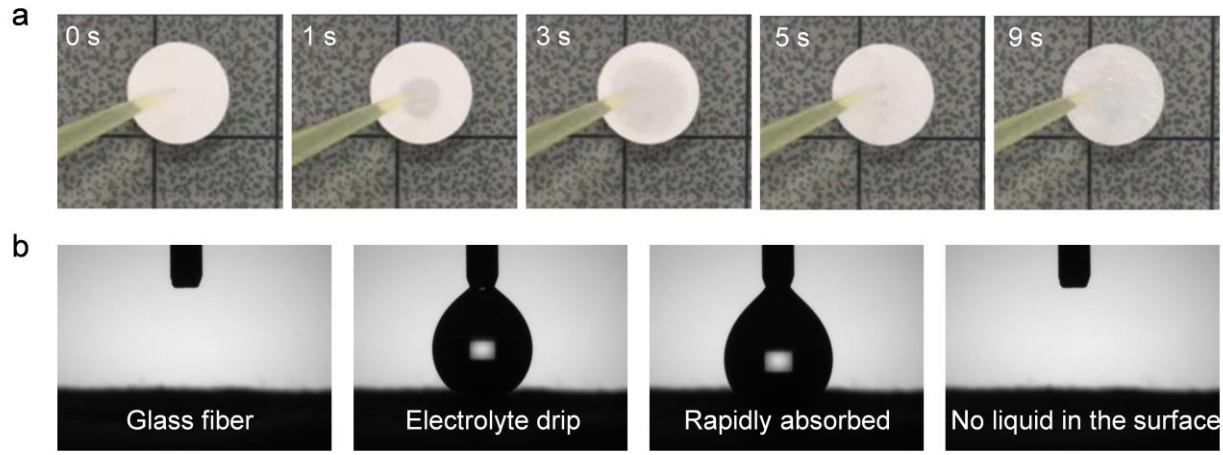

Fig. S7. Wetting property of GF separator with 2M $ZnSO_4$ aqueous electrolyte. (a) the digital photo. (b) The contact angles. The contact angle of liquid aqueous electrolyte with GF separator is extremely small to be observed and the liquid would soon be absorbed into the thick and porous fiber structures.

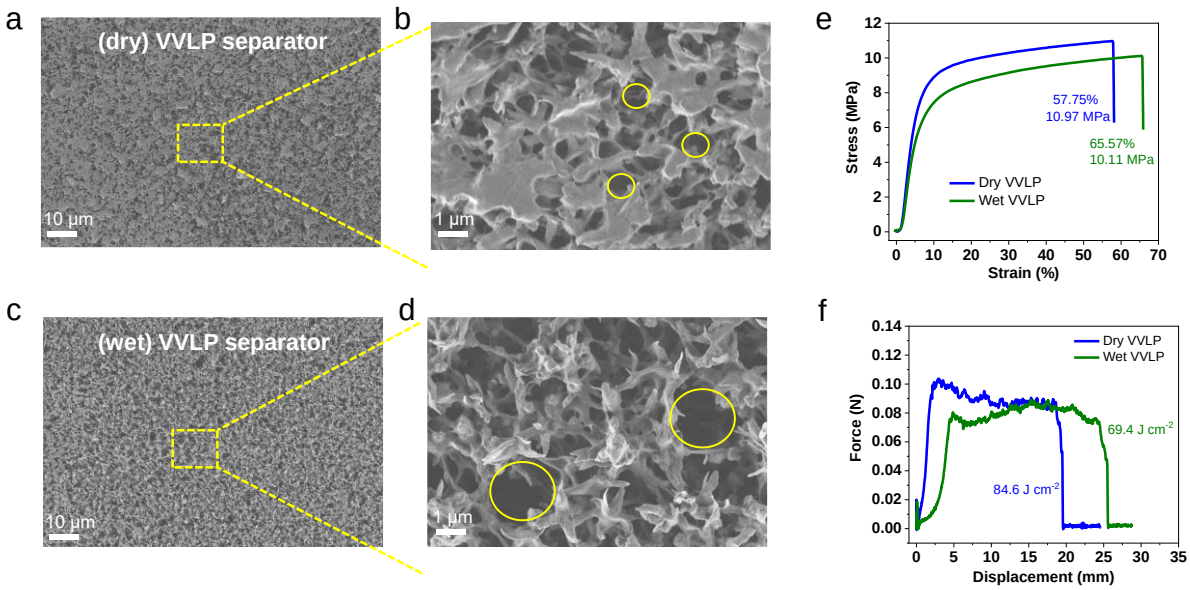

Fig. S8. SEM observation and mechanical properties of VVLP separator under dry and wet state. SEM picture of VVLP under dry state (a-b) and wet state (c-d). (e) Loading curves of VVLP separator under uniaxial elongation. (f) Tearing toughness of VVLP separator.

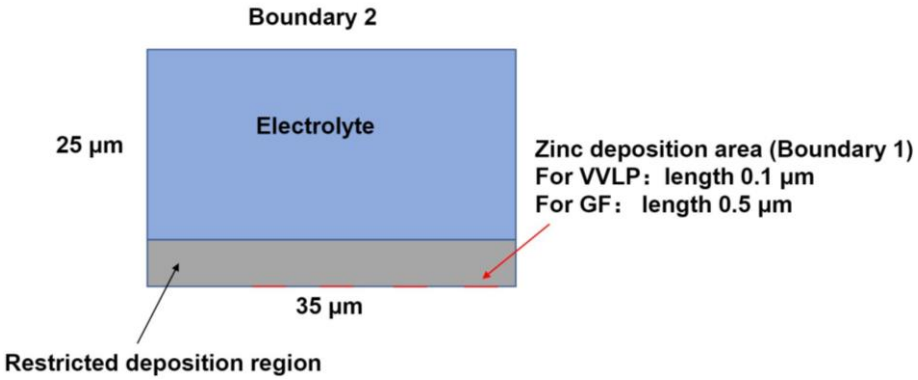

Fig. S9. The geometric model of COSMAL simulation in Zn batteries with glass fiber or VVLP separators.

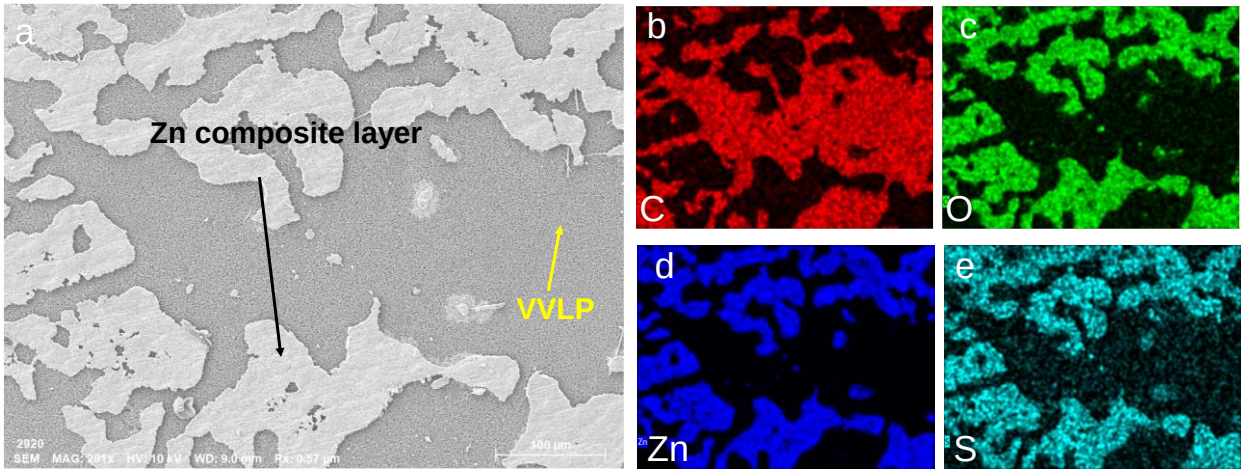

Fig. S10. VVLP separator with composite layer. (a) SEM images. (b-e) belongs to element mapping of C, O, Zn and S, respectively.

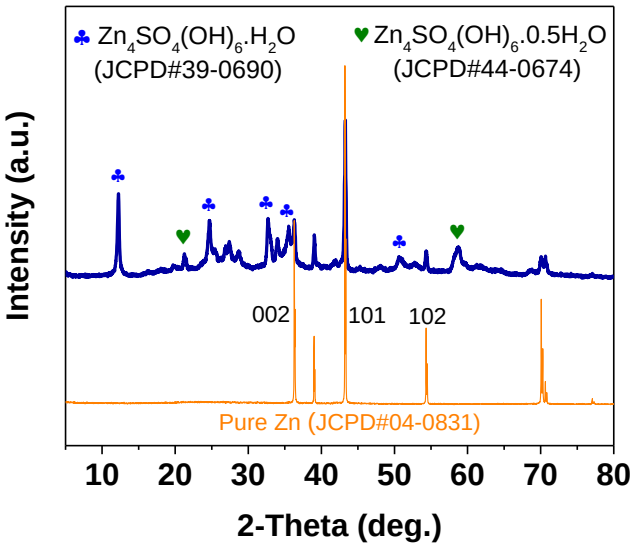

Fig. S11. XRD peak with main product of zinc sulfate hydroxide hydrate with tiny Zn particle in the composite layer adhering on VVLP separator surface.

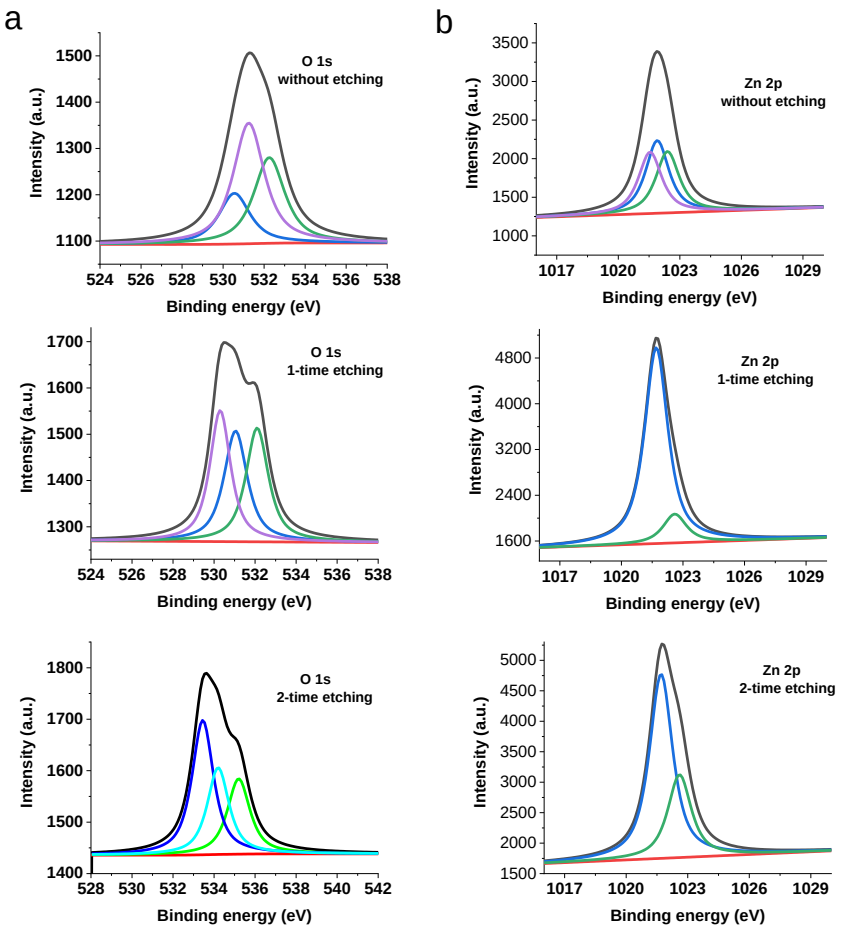

Fig. S12. XPS spectra of composite layer (a) O 1s spectra. (b) Zn 2p spectra. Similar to S 2p spectra, the O and Zn element distribution further verified the existence of ZSH composite layer.

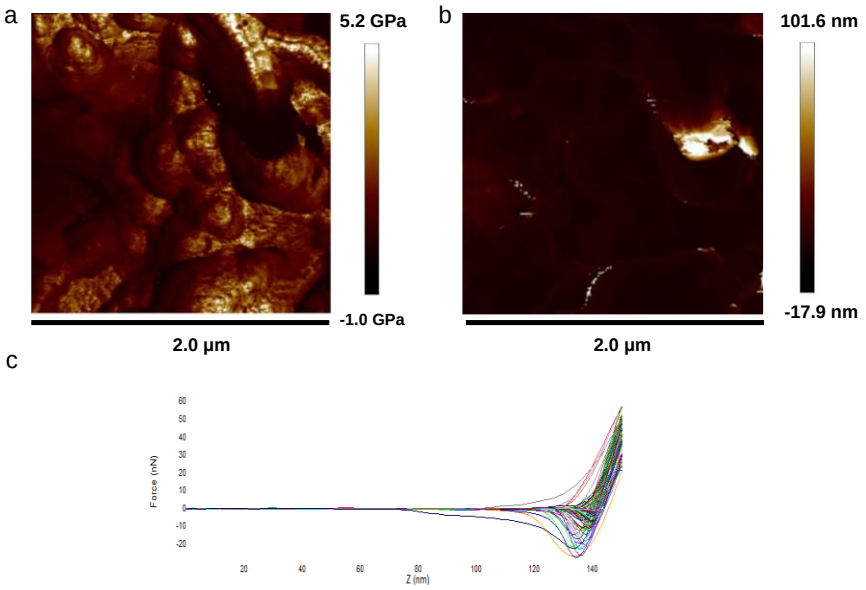

Fig. S13. AFM nanoindentation analysis of composite layer. (a) Two-dimensional maps of DMT modulus. (b) Indentation depth. (c) Force-displacement curves.

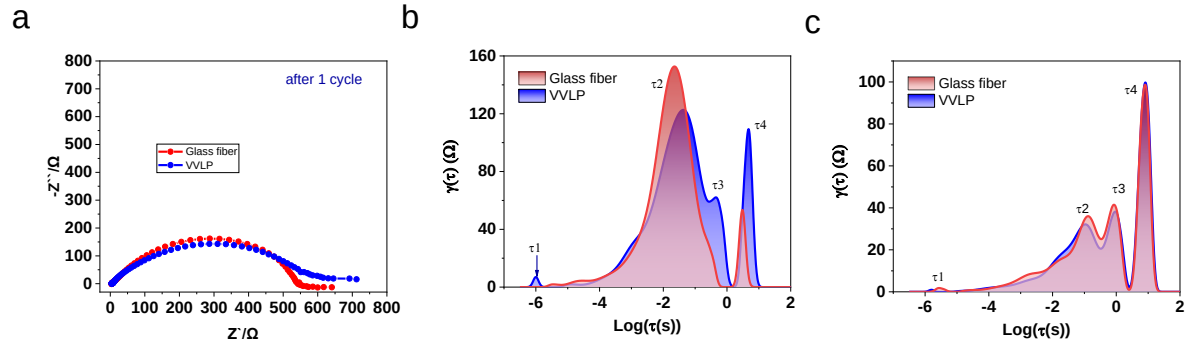

Fig. S14. EIS characterizations of Zn||Zn cells. EIS profiles after (a) 1 cycle and DRT profiles after (b) 1 cycle and (c) 10 cycles.

DRT analysis was conducted for better study the impedance at different frequencies. τ1, τ2, τ3, τ4 represents impedance in bulk of electrolyte, charge-transfer process, transfer in the interphase and Warburg, respectively. In the VVLP group, the forming of Zn composite layer did not cause considerable increase on each impedance.

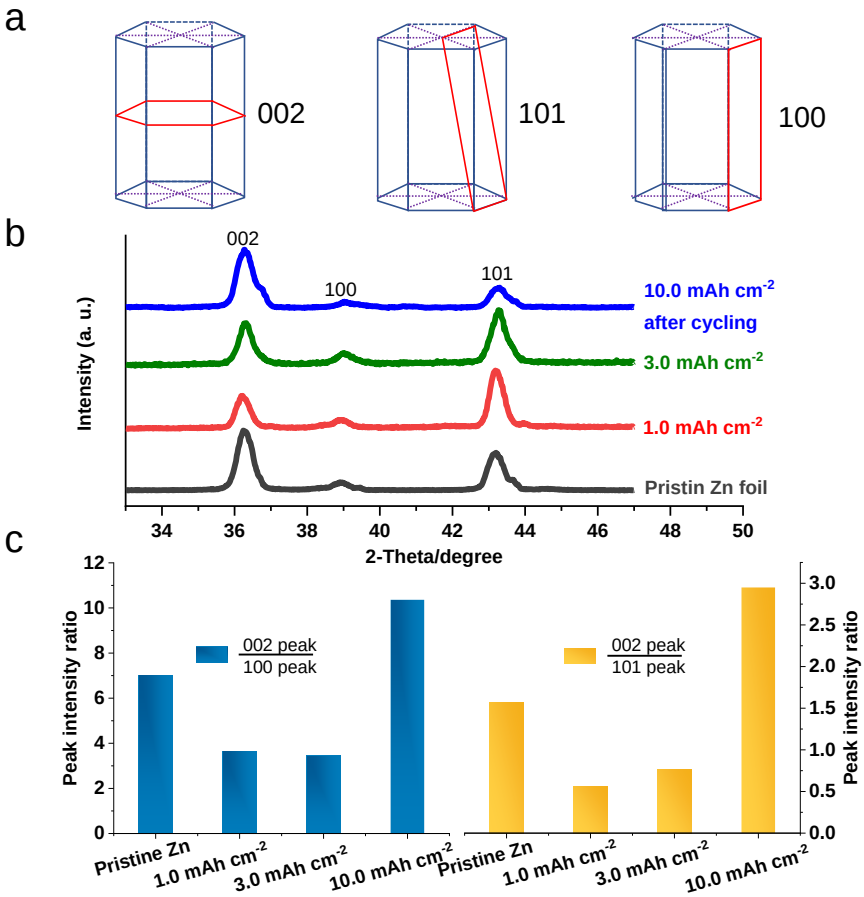

Fig. S15. Textures of Zn electrodeposition with VVLP separator under different states. (a) Three types of common Zn growth textures (002, 101, 100 plane). (b) XRD patterns of Zn electrodeposition with different capacity. (c) Peak intensity ratio of (002 peak)/(100 peak) on the left, and (002 peak)/(101 peak) on the right.

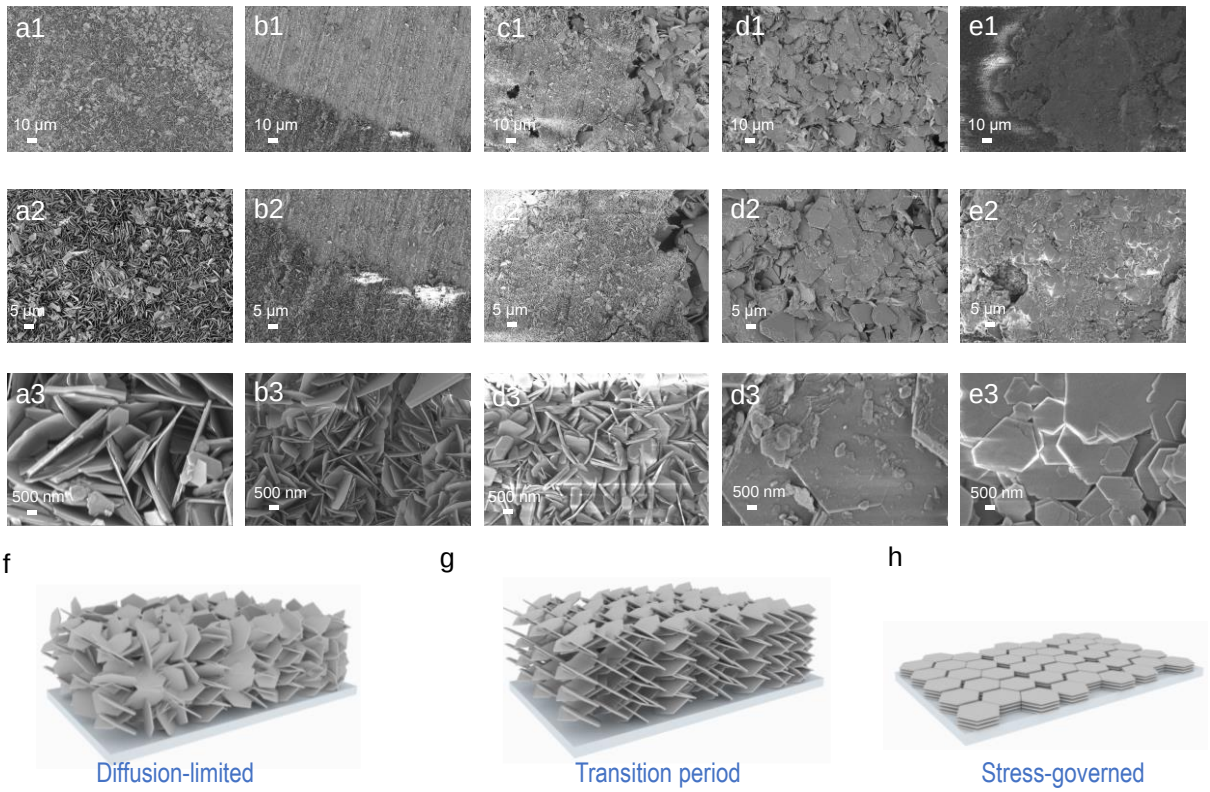

Fig. S16. SEM images and schematical illustration of Zn electrodeposition with VVLP separator under different states. Electrodeposition capacity (a1-a3) 0.25 mAh cm^{-2}, (b1-b3) 1.0 mAh cm^{-2}, (c1-c3) 3.0 mAh cm^{-2}, (d1-d3) 10.0 mAh cm^{-2}, Current density, C=1.0 mA cm^{-2}. (e1-e3) 20.0 mAh cm^{-2}, Current density, C=10.0 mA cm^{-2}. Schematical illustration of Zn electrodeposition. (f) Almost vertical angle growth by diffusion-limited aggregation. (g) Slight flat angle growth in transitional period. (h) In-planar growth with stress-governed mechanism.

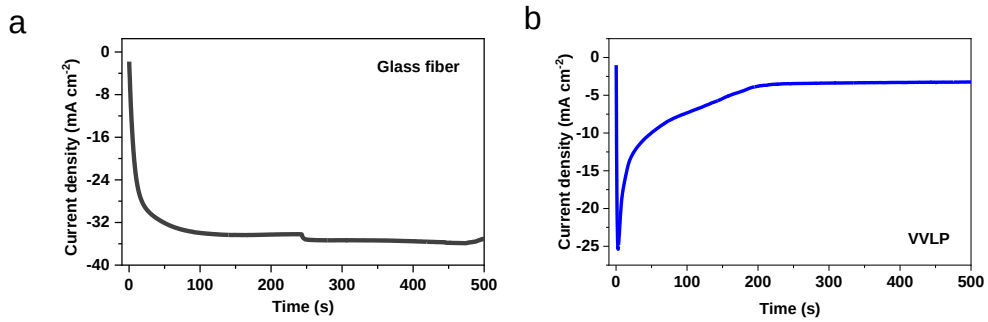

Fig. S17. Chronoamperograms of Zn plates working under −0.15 V within 300 s with (a) glass fiber separator and (b) VVLP separator.

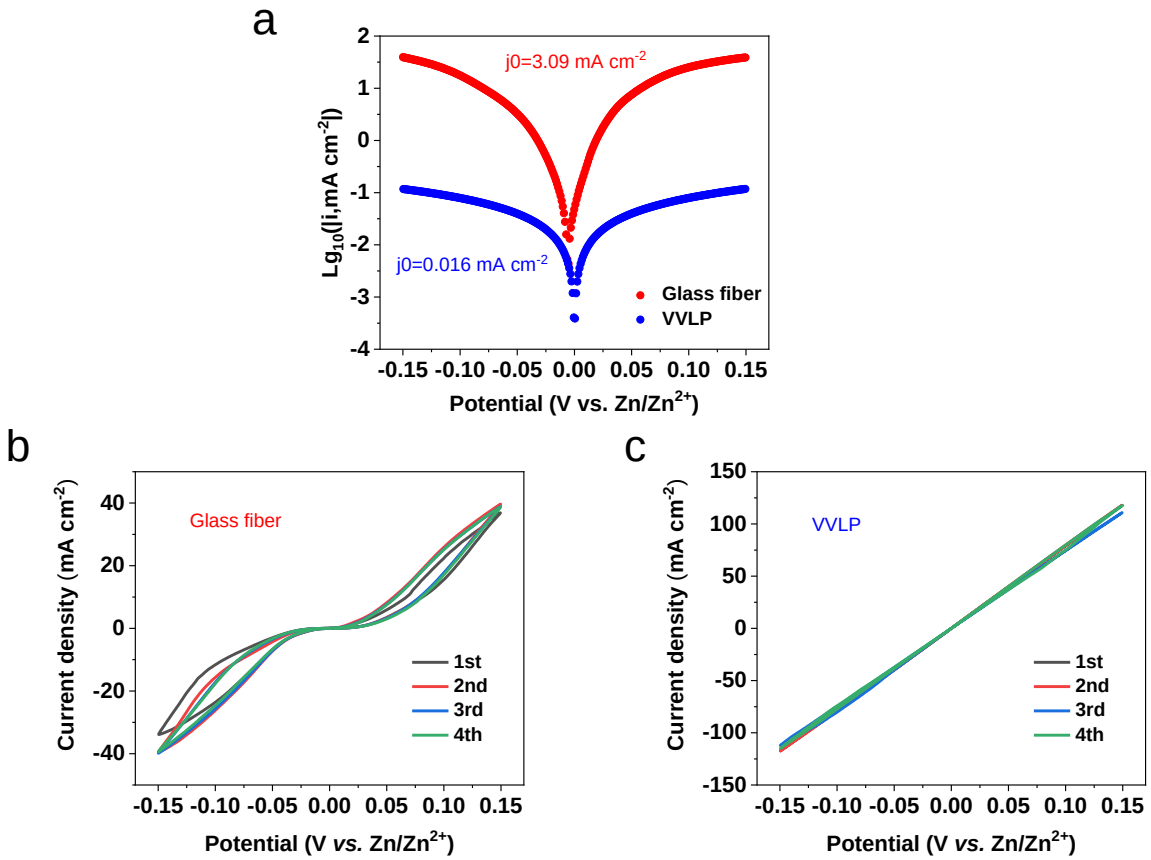

Fig. S18. (a) Linear polarization curves for describing the corrosion of Zn anodes. Current density profiles in the linear polarization for the cell with glass fiber (b) and VVLP separators (c).

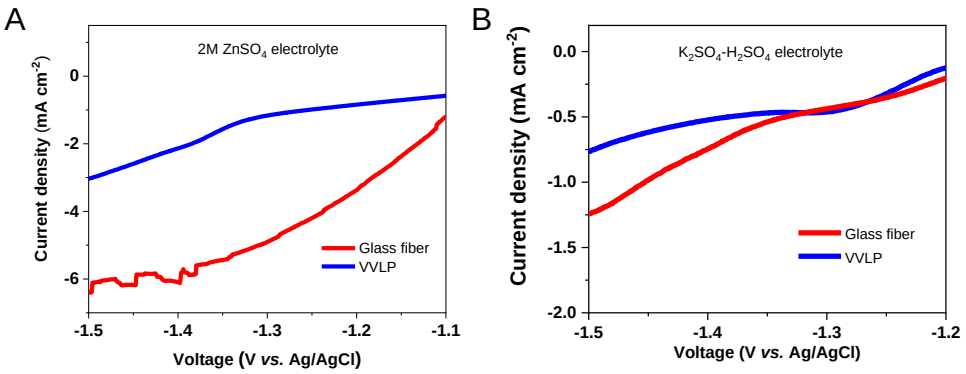

Fig. S19. LSV of three electrodes cell to determine cathodic current density of HER at 5 mV s^{-1} in (a) 2M ZnSO4 electrolyte and (b) pH-equivalent K_2SO_4-H_2SO_4 electrolyte.

Fig. S19a gives the linear sweep voltammetry in 2M $ZnSO_4$ electrolyte, where the cathodic current was attributed to the sum of HER and Zn reduction. In view of the high dependence of H_2 evolution kinetics on the activity of H^+ in electrolyte, we then formulated a pH-equivalent K_2SO_4-H_2SO_4 electrolyte to eliminate the interference of Zn reduction. This electrolyte was solely adopted to study the HER behaviors by eliminating the effect of Zn reduction. In such cases, there is no Zn reduction process, and any cathodic current signal can be ascribed to H_2 formation. In a contrast, there is an obvious lower current of HER for VVLP group, which indicates its effectiveness of suppressing HER.

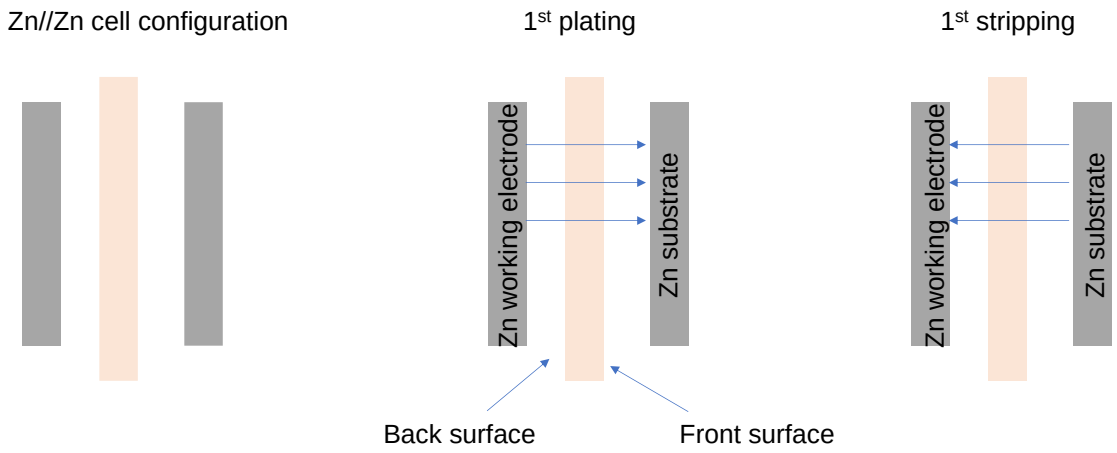

Fig. S20. Illustration of Zn//Zn symmetric cell configuration to define the back surface and front surface.

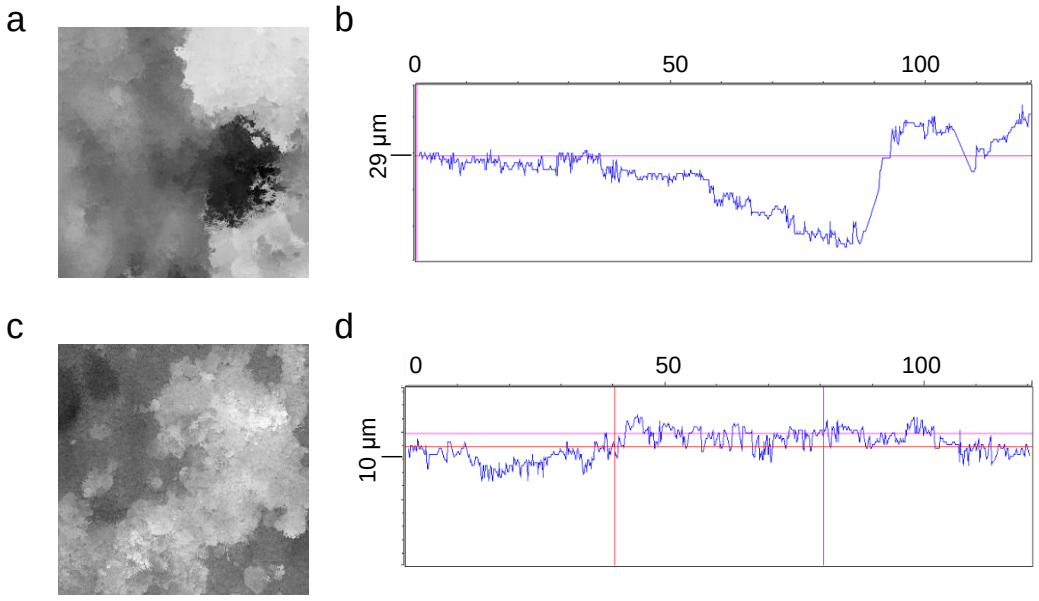

Fig. S21. LSCM test of Zn plates cycled in different separators. The selected region for LSCM characterization of the Zn plate cycled with (a) glass fiber separator and (c) VVLP separator. The height evolution profiles of Zn plate cycled with (b) glass fiber separator and (d) VVLP separator.

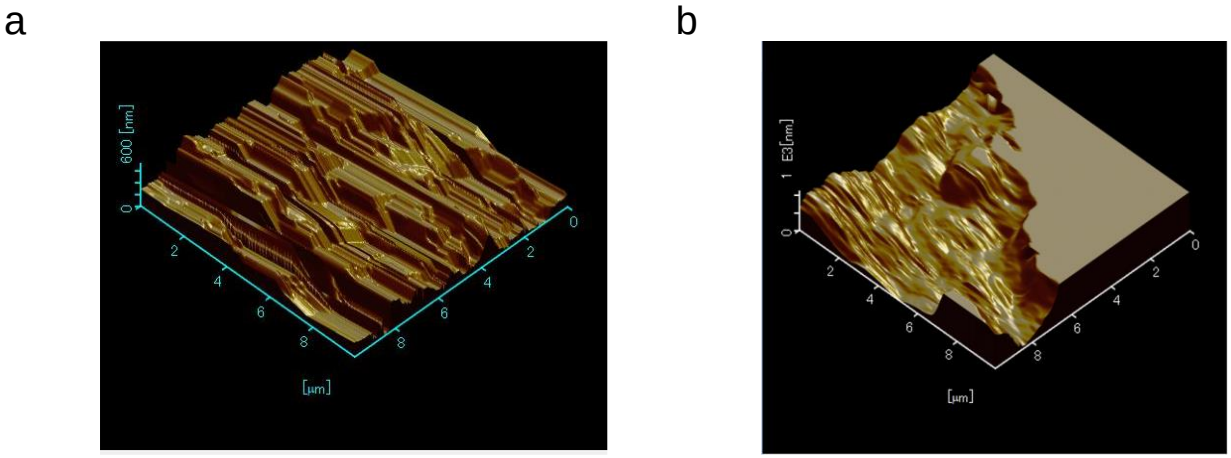

Fig. S22. AFM characterization of Zn plates. AFM images of Zn plate cycled with (a) glass fiber separator and (b) VVLP separator.

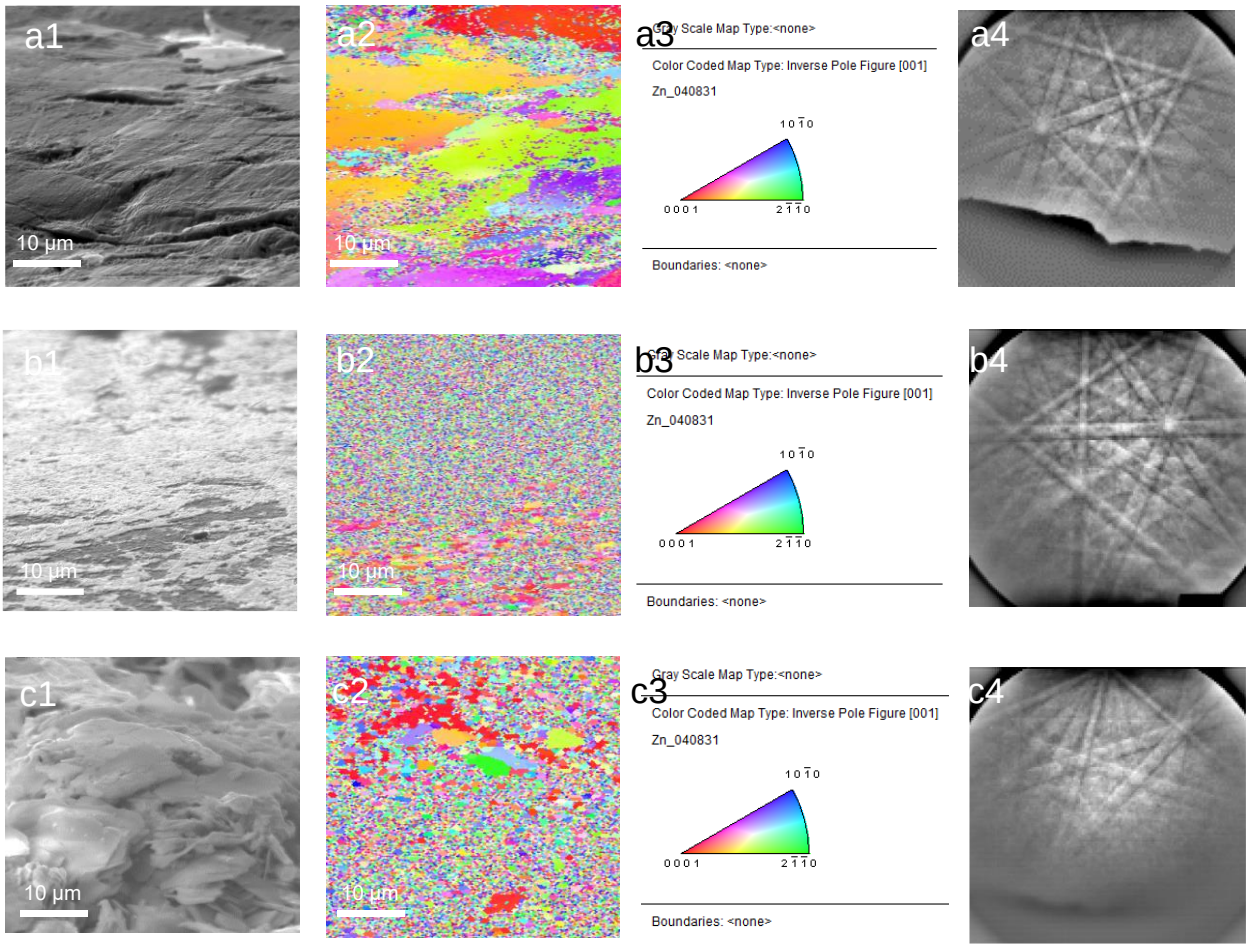

Fig. S23. EBSD characterization of Zn plates. Sample **a**, **b and c** is pristine Zn, Zn plate after cycle with glass fiber separator and external stress from hydraulic pressure, Zn plate work with VVLP separator, respectively. The figures from left to right are selected SEM images, corresponding EBSD map, orientation map and related Kikuchi pattern.

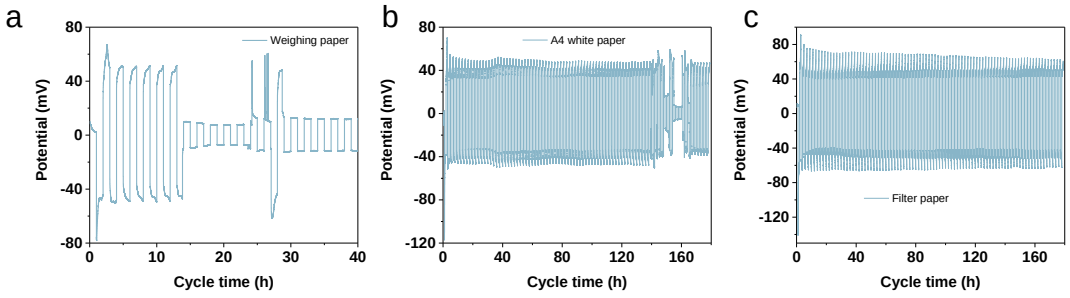

Fig. S24. Symmetric Zn cells with different separators at 1.0 mA cm^{-2} and 1.0 mAh cm^{-2}, (a) weighing, (b) A4 white paper, (c) Filter paper.

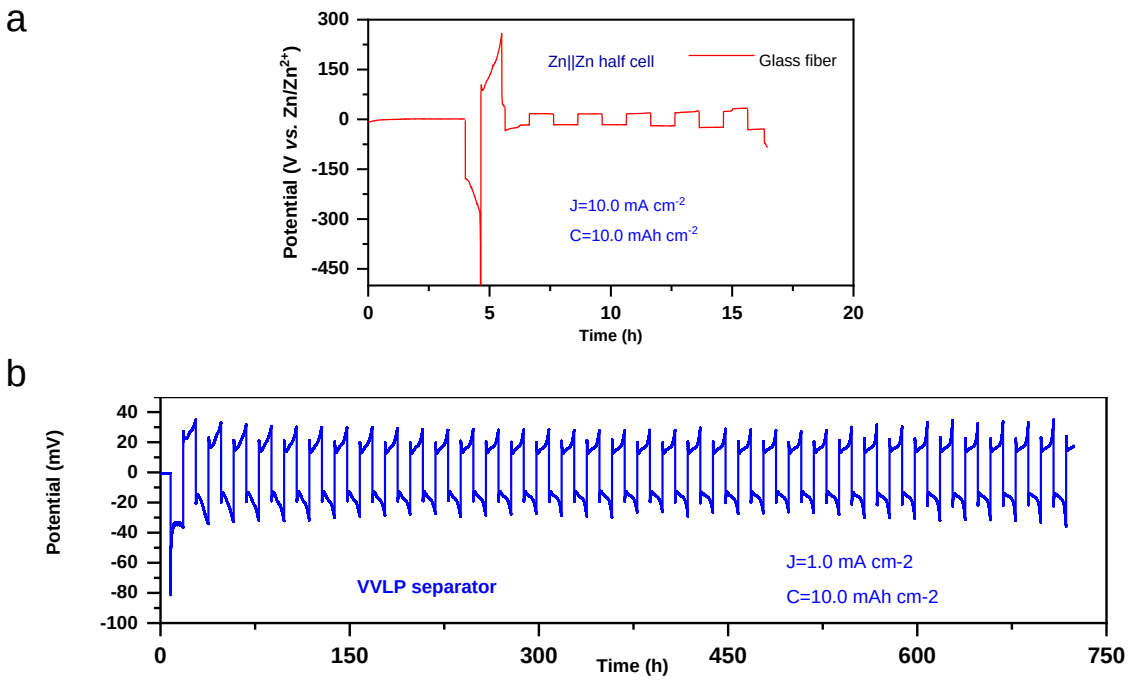

Fig. S25. Symmetric Zn cell with GF separator (a) at 10.0 mA cm^{-2} and 10.0 mAh cm^{-2}, (b) with VVLP separator at 1.0 mA cm^{-2} and 10.0 mAh cm^{-2}.

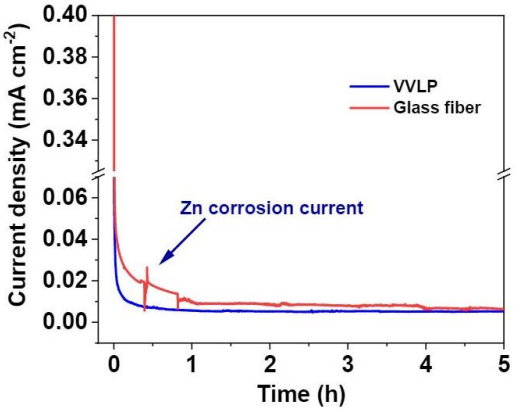

Fig. S26. Galvanic corrosion of Zn-Cu half cell with glass fiber or VVLP separators.

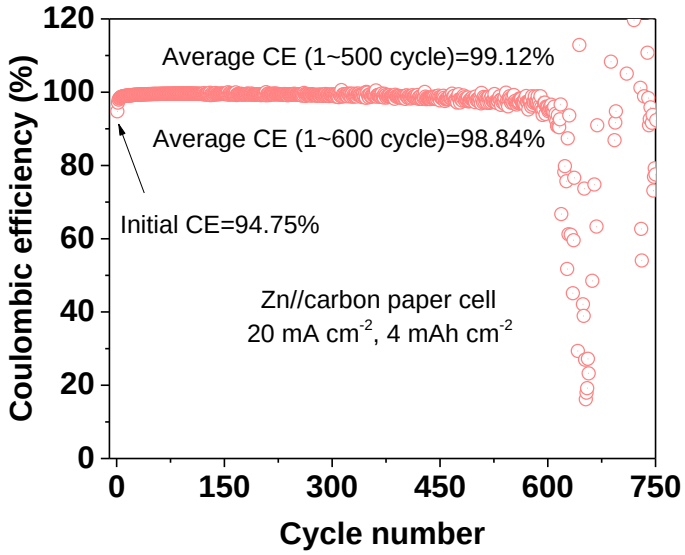

Fig. S27. Zn plating/stripping efficiency on carbon paper substrate with glass fiber separator.

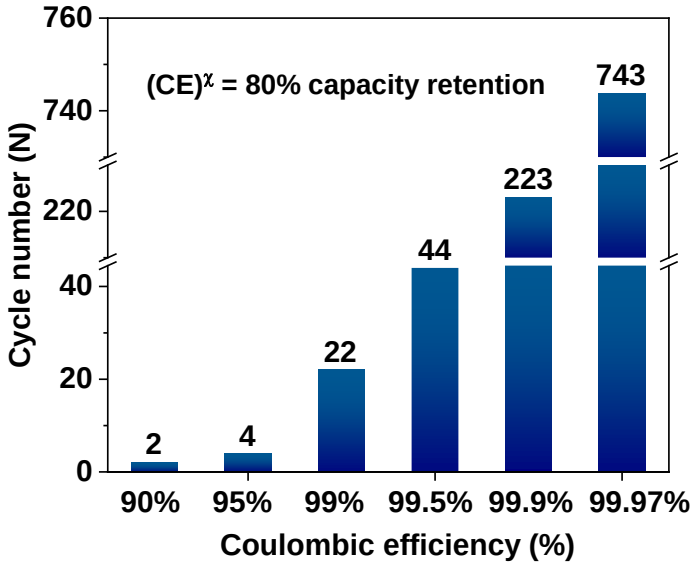

Fig. S28. The Zn battery lifespan calculation (80% capacity retention) based on the electrodeposition-dissolution CE values (the Zn loss source).

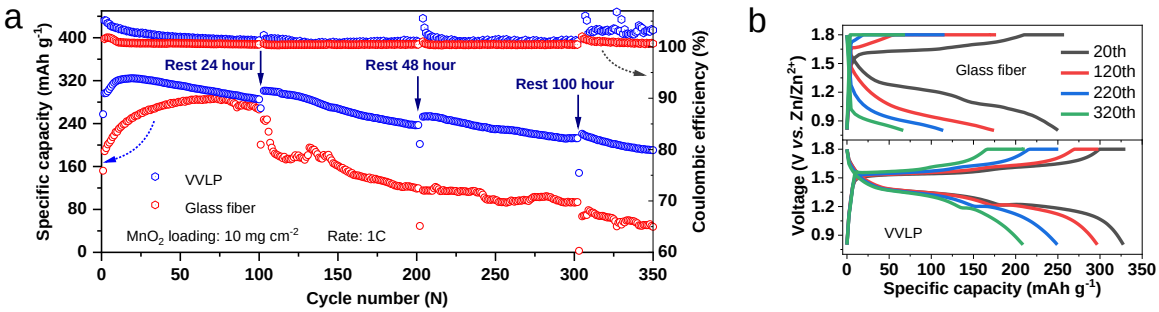

Fig. S29. (a) Cycle performance and the corresponding CE of Zn-MnO_2 coin cells (MnO_2 loading: 10 mg cm^{-2}) with GF or VVLP separator at 1C=308 mAh g^{-1} with different resting time of 24, 48 and 100 h after 100, 200, 300 cycles, respectively. (b) The discharge-charge voltage curves of cells with GF (top) and VVLP separator (bottom) at 20, 120, 220 and 320 cycles, respectively.

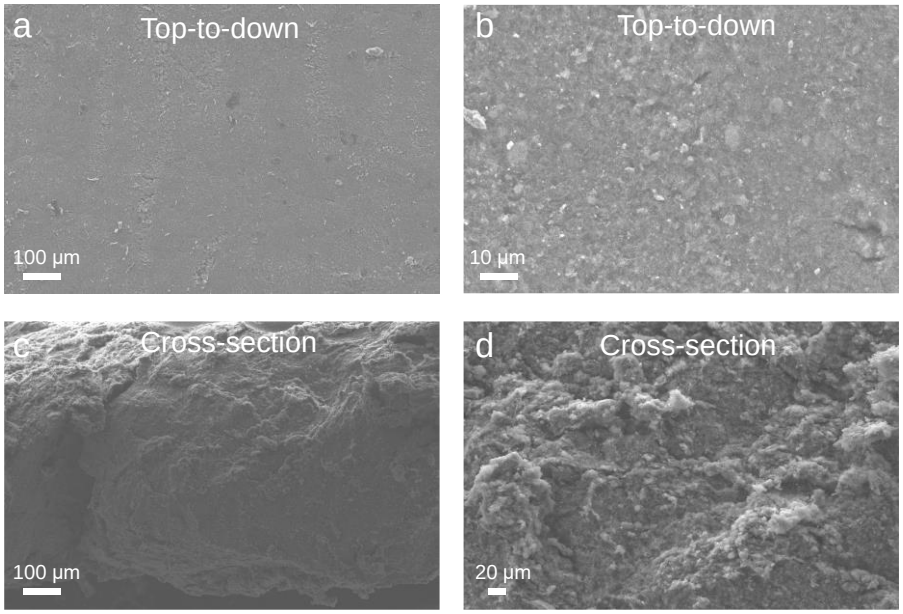

Fig. S30. SEM observation of pristine high-loading MnO2 electrode. (a-b) Top-to-down. (b) Cross-section.

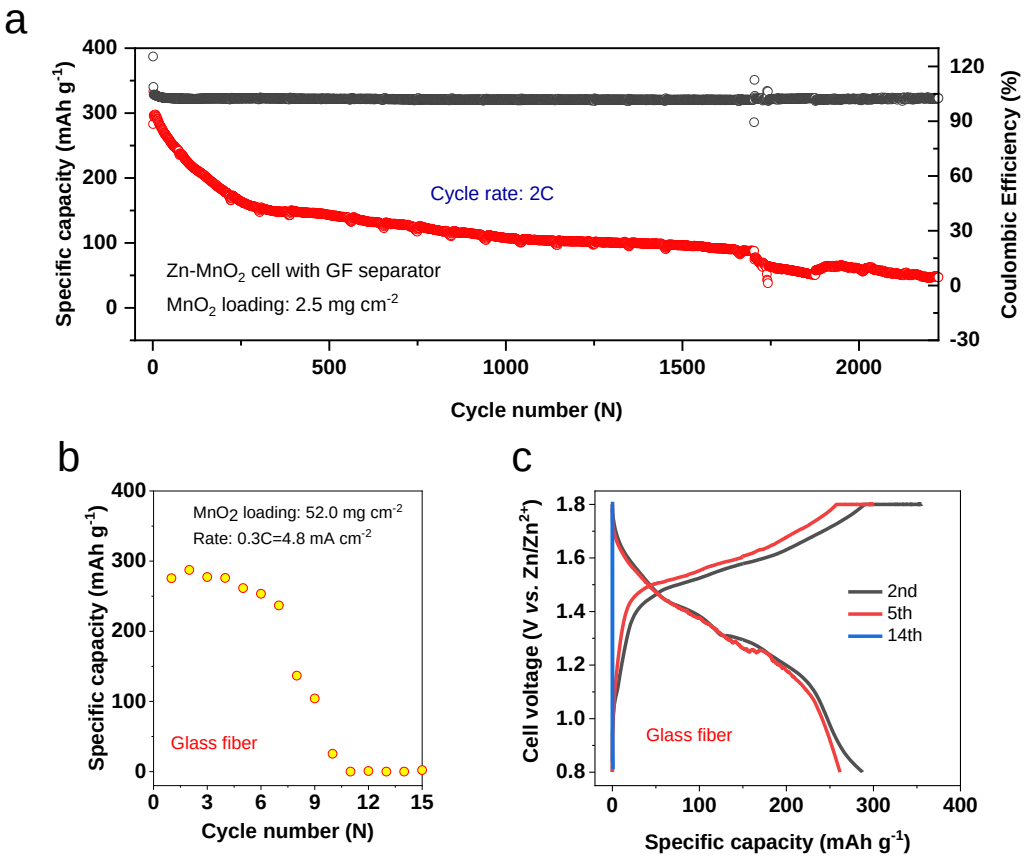

Fig. S31. Cycle performance of Zn-MnO_2 coin cells with glass fiber separator. (a) Cycle performance of Zn-MnO_2 battery over 2000 cycles with thin MnO_2 electrode (2.5 mg cm^{-2}) and excessive Zn anode (100 μm). (b) The cell with thick MnO_2 electrode (52.0 mg cm^{-2}). (c) Corresponding voltage profiles.

fig. S31a showcases the cycle performance with thin MnO_2 electrode over 2000 cycles, which represents most of previous reports. When pairing with excessive Zn electrode, the coin-cell performance cannot truly reveal the failure mechanism and the protection effectiveness of Zn metal anode. Therefore, the fast capacity decay in cell with thick MnO_2 electrode demonstrates the poor Zn protection in glass fiber separator group. The Zn anode electrodeposition-dissolution at high capacity and high current density remains a threat for the development of high-energy Zn batteries toward future real-world applications.

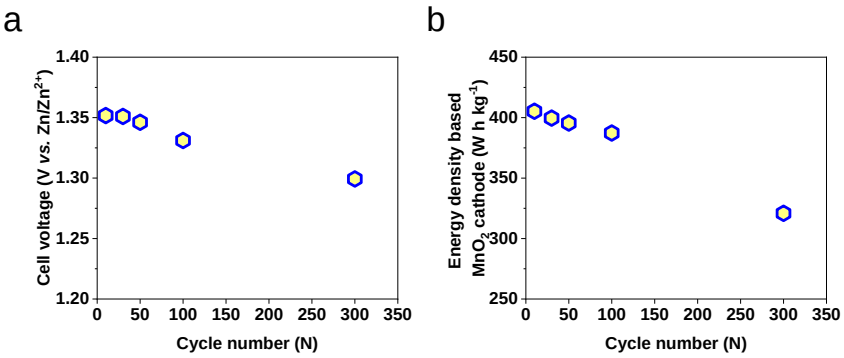

Fig. S32. Cycle performance of high-capacity Zn||MnO_2 coin cell (MnO_2 loading: 52 mg cm^{-2}) with VVLP separator. The evolution of (a) average discharge voltage and (b) Energy density based on MnO_2 cathode.

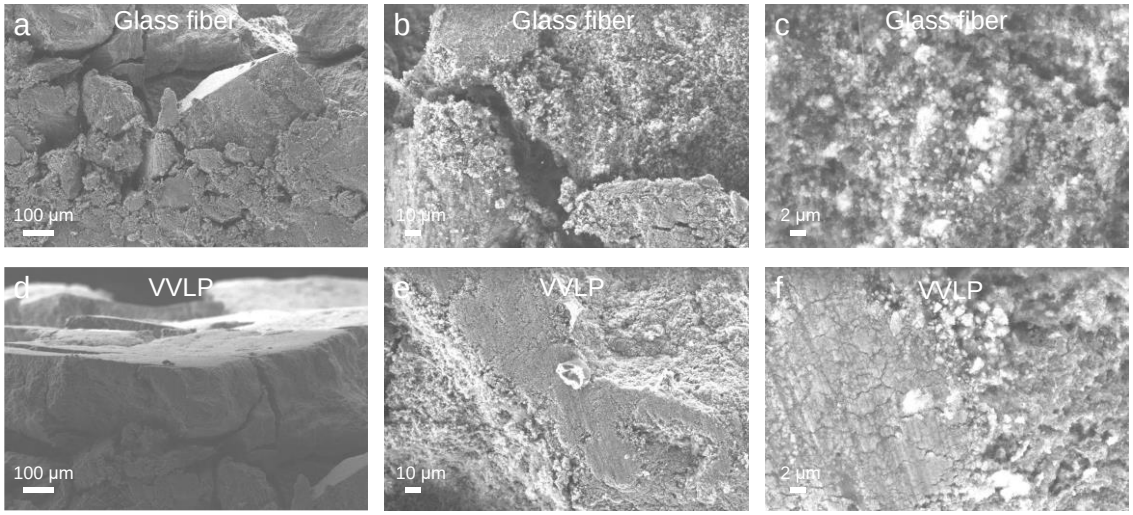

Fig. S33. Cross-section SEM observation of MnO_2 electrode after cycling with different separators. (a-c) Glass fiber. (d-f) VVLP separator.

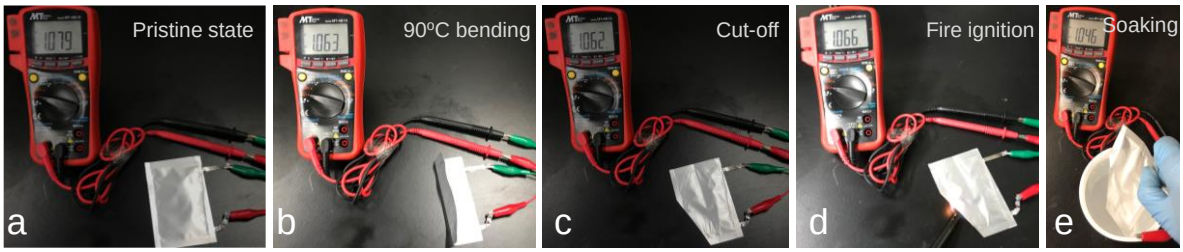

Fig. S34. Voltage evolution of pouch cell at pristine (a), 90°C bending (b), 1/4 cut-off (c), fire ignition (d) and even following soaking into water (e), respectively.

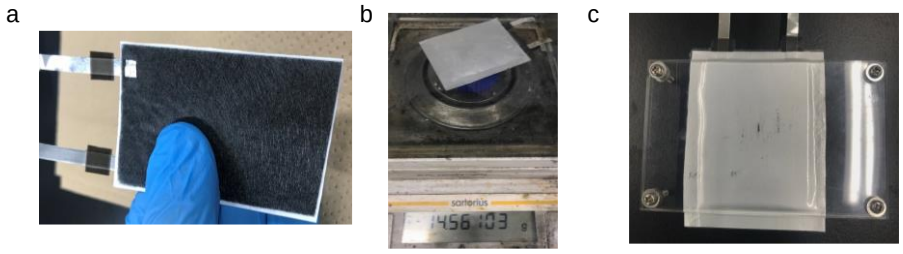

Fig. S35. Pouch cell assembling. (a) Optical picture of one-layer pouch cell assembling. (b) Weight of pouch cell. (c) Cycle condition of pouch cell. The detailed parameter is illustrated the Supplementary Table 3.

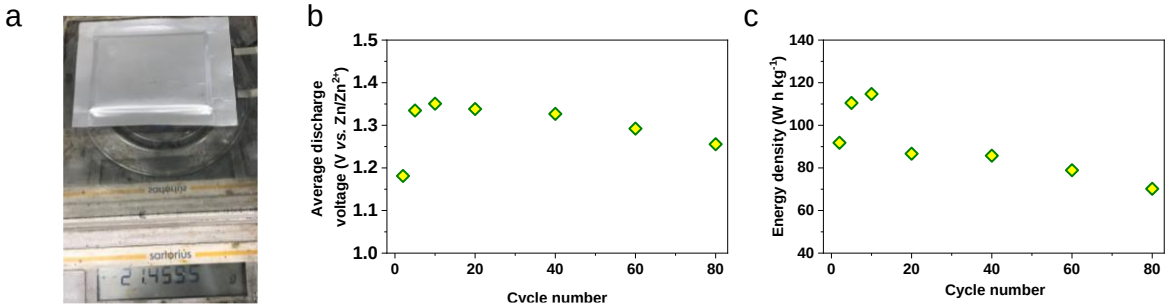

Fig. S36. (a) Optical picture of three-layer pouch cell wight. The evolution of (b) average discharge voltage and (c) Energy density based on pouch cell level. The detailed parameter is illustrated the Supplementary Table 4.

Supplementary Tables

Table S1. Mechanical properties of Glass fiber and VVLP separators

Separator types	Breaking point & Pressure (MPa)	Shear Modulus (MPa)	Young`s Modulus (MPa)	Tearing toughness (J cm^{-2})
Glass fiber	3.85%, 0.18 MPa	/	/	15.8
Dry VVLP	57.75%, 10.97 MPa	45.8	137.4	84.6
Wet VVLP	65.57%, 10.11 MPa	34.2	102.6	69.4

Table S2. Literature survey of strategies for Zn metal anode protection

Strategies	Performance of Zn||Zn cell, lifespan (h) and current density (mA cm^{-2})	Efficiency of Zn plating/stripping under current density and capacity (mA cm^{-2}, mAh cm^{-2}, %)	Ref.
VVLP separator (2 mol $ZnSO_4$)	**4900 h, 1.0 mA cm^{-2}; 2400 h, 3.0 mA cm^{-2}; 280 h, 10.0 mA cm^{-2};**	**2.0, 2.0, 99.93% 10.0 1.0, 99.75% 20.0, 4.0, 99.97%**	**This work**
Metal-organic framework membrane (2 mol $ZnSO_4$)	3000 h, 0.2 mA cm^{-2}; 700 h, 2.0 mA cm^{-2}; 350 h, 5.0 mA cm^{-2};	/	[1]
Molecular zeolite sieve composite electrolyte (2 mol $ZnSO_4$)	4765 h, 0.8 mA cm^{-2}; 430 h, 2.0 mA cm^{-2}; 310 h, 2.5 mA cm^{-2};	/	[2]
MOF-based single-ion Zn^{2+} solid electrolyte	350 h, 0.1 mA cm^{-2}	/	[3]
Graphene oxide-based separator (2 mol $ZnSO_4$)	1750 h, 2.0 mA cm^{-2}; 400 h, 20.0 mA cm^{-2};	1.0 1.0, 98.69%	[4]
Graphene coating (2 mol $ZnSO_4$)	/	40.0, 1.6, 99.9%; 40.0, 3.2, 99.7%;	[5]
Carbon nanotube matrix (2 mol $ZnSO_4$)	200 h, 2.0 mA cm^{-2}; 100 h, 5.0 mA cm^{-2};	2.0, 2.0, ~97%; 5.0, 2.0, 97.9%;	[6]
Zincophilic carbon host 3 mol $Zn(CF_3SO_3)_2$	116.7 h, 0.5 mA cm^{-2};	1.0, 4.0, ~95%;	[7]
Solid-polymer electrolyte	1500 h, 2.0 mA cm^{-2};	0.5, 0.5, 99.36%	[8]
Metal-organic framework coating (2 mol $ZnSO_4$)	3000 h, 0.5 mA cm^{-2};	/	[9]
Inorganic $CaCO_3$ Coatings (3 mol $ZnSO_4$+0.1 mol $MnSO_4$)	800 h, 0.25 mA cm^{-2}	/	[10]
Cerium-based film (2 mol $ZnSO_4$+0.1 mol $MnSO_4$)	1200 h, 4.4 mA cm^{-2}	1.13, 0.57, 99.1%;	[11]
ZnS interphase coating	1000 h, 2.0 mA cm^{-2}	2.0, 1.0, 99.2%	[12]
High-concentrated electrolyte (1 mol $Zn(TFSI)_2$+20 mol LiTFSI/H_2O	170 h, 0.2 mA cm^{-2}	1.0 mA cm^{-2}, Ave. CE=99.9%	[13]
High-concentrated electrolyte 30 mol $ZnCl_2/H_2O$	600 h, 0.2 mA cm^{-2}	0.2 mA cm^{-2}, Ave. CE=95.4%	[14]
Organic electrolyte 0.5 mol $Zn(OTf)_2$/TMP	2400 h, 1.0 mA cm^{-2}	0.5, 0.5, 99.57%	[15]
Organic electrolyte 0.5 mol $Zn(OTf)_2$/TEP	2000 h, 0.5 mA cm^{-2}	0.5, 0.5, 99.68%	[16]
Organic electrolyte 0.5 mol $Zn(OTf)_2$/DMF	2700 h, 1.0 mA cm^{-2}	1.0, 1.0, 99.8%	[17]
4 m $Zn(OTF)_2$+0.5 m $Me_3EtNOTF/H_2O$	6000 h, 0.5 mA cm^{-2}	0.5, 0.5, >99.0%	[18]
Solid poly(1,3-dioxolane) electrolytes	1800 h, 1.0 mA cm^{-2}	0.5, 0.5, 99.7%	[19]
Ethylene Glycol-added aqueous electrolyte	1200 h, 1.0 mA cm^{-2}	/	[20]

Methanol-added aqueous electrolyte	/	1.0, 0.5, 99.7%	[21]

Table S3. Cell parameters for the one-layer pouch cell.

Electrochemical parameter	Values	Physical parameter	Value
Specific capacity	284.2 mAh g^{-1}	Zn anode (100 μm)	2.501 g
Cell average voltage	1.34 V	Weight of cathode	6.825 g
Capacity	517.3 mAh	Carbon paper weight	0.902 g
Energy	0.693 W h	Electrolyte weight	8.623g
Active area	35.0 cm^2	Separator weight	0.220
Energy density	47.6 W h kg^{-1}	Package + Tabs weight	1.38 g
		Pouch-cell weight	14.561

Table S4. Cell parameters for the three-layer pouch cell.

Electrochemical parameter	Values	Physical parameter	Value
MnO_2 ratio (*vs.* cathode)	80%	Composite anode (Zn + carbon paper)	3.093 g
Specific capacity	319.2 mAh g^{-1}	Weight of cathode	6.825 g
Cell average voltage	1.35 V	Carbon paper (positive current collector)	0.902 g
Capacity	1.83 Ah	Electrolyte weight	8.501g
Energy	2.47 W h	Separator weight	0.658
Energy density	115.1 W h kg^{-1}	Package + Tabs weight	1.480 g
		Pouch-cell weight	21.459

Table S5. Literature survey of high-capacity Zn-MnO_2 batteries

Strategies	Areal-capacity (mAh cm^{-2})	Coin-cell performance (N/P ratio, cycles, retention)	Pouch-cell performance (N/P ratio, cycles, retention, energy density (W h/kg))	Ref.
VVLP separator (2 mol $ZnSO_4$+0.1 mol $MnSO_4$)	**17.4**	**(3.74, 350 cycles, 80%)**	**(1.35, 80, 79%, 115.1)**	**This work**
Nanocarbon layer 3 mol $Zn(CF_3SO_3)_2$+0.1 mol $Mn(CF_3SO_3)_2$	/	1.0, 80 cycles, 68.2%	/	[22]
KI-redox mediator (KI added $ZnSO_4$ electrolyte)	2.5	/, 400 cycles, >99%	/	[23]
Graphene coated Zn (2 mol $ZnSO_4$+0.1 mol $MnSO_4$)	0.8	2, 1000 cycles, 65%	/	[5]
ZnF_2-coated Zn (2 mol $ZnSO_4$+0.1 mol $MnSO_4$)	3	(/, 1000 cycle, 93.63%)	(/, 160, 93.17%, /)	[24]

References:

1. H. Yang, Y. Qiao, Z. Chang, H. Deng, P. He and H. Zhou, *Adv. Mater.*, 2020, **32**, 2004240.
2. H. Yang, Y. Qiao, Z. Chang, H. Deng, X. Zhu, R. Zhu, Z. Xiong, P. He and H. Zhou, *Adv. Mater.*, 2021, **33**, 2102415, e2102415.
3. Z. Wang, J. Hu, L. Han, Z. Wang, H. Wang, Q. Zhao, J. Liu and F. Pan, *Nano Energy*, 2019, **56**, 92-99.

4. J. Cao, D. Zhang, C. Gu, X. Wang, S. Wang, X. Zhang, J. Qin and Z. S. Wu, *Adv. Energy Mater.*, 2021, **11**, 2101299.
5. J. Zheng, Q. Zhao, T. Tang, J. Yin, C. D. Quilty, G. D. Renderos, X. Liu, Y. Deng, L. Wang and D. C. Bock, *Science*, 2019, **366**, 645-648.
6. Y. Zeng, X. Zhang, R. Qin, X. Liu, P. Fang, D. Zheng, Y. Tong and X. Lu, *Adv. Mater.*, 2019, **31**, 1903675.
7. F. Xie, H. Li, X. Wang, X. Zhi, D. Chao, K. Davey and S. Z. Qiao, *Adv. Energy Mater.*, 2021, **11**, 2003419.
8. L. Ma, S. Chen, N. Li, Z. Liu, Z. Tang, J. A. Zapien, S. Chen, J. Fan and C. Zhi, *Adv. Mater.*, 2020, **32**, 1908121.
9. H. Yang, Z. Chang, Y. Qiao, H. Deng, X. Mu, P. He and H. Zhou, *Angew. Chem.*, 2020, **59**, 9377-9381.
10. L. Kang, M. Cui, F. Jiang, Y. Gao, H. Luo, J. Liu, W. Liang and C. Zhi, *Adv. Energy Mater.*, 2018, **8**, 1801090.
11. C. Deng, X. Xie, J. Han, B. Lu, S. Liang and J. Zhou, *Adv. Funct. Mater.*, 2021, **31**, 2103227.
12. J. Hao, B. Li, X. Li, X. Zeng, S. Zhang, F. Yang, S. Liu, D. Li, C. Wu and Z. Guo, *Adv. Mater.*, 2020, **32**, 2003021.
13. F. Wang, O. Borodin, T. Gao, X. Fan, W. Sun, F. Han, A. Faraone, J. A. Dura, K. Xu and C. Wang, *Nat. Mater.*, 2018, **17**, 543-549.
14. C. Zhang, J. Holoubek, X. Wu, A. Daniyar, L. Zhu, C. Chen, D. P. Leonard, I. A. Rodriguez-Perez, J. X. Jiang, C. Fang and X. Ji, *Chem. Commun.*, 2018, **54**, 14097-14099.
15. A. Naveed, H. Yang, Y. Shao, J. Yang, N. Yanna, J. Liu, S. Shi, L. Zhang, A. Ye, B. He and J. Wang, *Adv. Mater.*, 2019, **31**, 1900668.
16. A. Naveed, H. Yang, J. Yang, Y. Nuli and J. Wang, *Angew. Chem.*, 2019, **58**, 2760-2764.
17. N. Wang, X. Dong, B. Wang, Z. Guo, Z. Wang, R. Wang, X. Qiu and Y. Wang, *Angew. Chem.*, 2020, **132**, 14685-14691.
18. L. Cao, D. Li, T. Pollard, T. Deng, B. Zhang, C. Yang, L. Chen, J. Vatamanu, E. Hu, M. J. Hourwitz, L. Ma, M. Ding, Q. Li, S. Hou, K. Gaskell, J. T. Fourkas, X. Q. Yang, K. Xu, O. Borodin and C. Wang, *Nat. Nanotechnol.*, 2021, **16**, 902-910.
19. L. Ma, S. Chen, X. Li, A. Chen, B. Dong and C. Zhi, *Angew. Chem.*, 2020, **59**, 23836-23844.
20. N. Wang, Y. Yang, X. Qiu, X. Dong, Y. Wang and Y. Xia, *ChemSusChem*, 2020, **13**, 5556-5564.
21. J. Hao, L. Yuan, C. Ye, D. Chao, K. Davey, Z. Guo and S. Z. Qiao, *Angew. Chem.*, 2021, **60**, 7366-7375.
22. Y. Zhu, Y. Cui and H. N. Alshareef, *Nano lett.*, 2021, **21**, 1446-1453.
23. J. Lei, Y. Yao, Z. Wang and Y.-C. Lu, *Energy Environ. Sci.*, 2021, **14**, 4418-4426.
24. L. Ma, Q. Li, Y. Ying, F. Ma, S. Chen, Y. Li, H. Huang and C. Zhi, *Adv. Mater.*, 2021, **33**, 2007406.